ACS OMEGA

Open Access

http://pubs.acs.org/journal/acsodf

Article

Hydrothermal Synthesis, Phase Analysis, and Magneto-Electronic Characterizations of Lead-Free Ferroelectric BM^{2+}(Zn, Ca, Mg)T−BFO System

K. Monower Hossain, M. H. Kabir Rubel,* M. Khalid Hossain,* G. F. Ishraque Toki, Latha Marasamy, Rajesh Haldhar,* Md Hasan Ali, Smriti Baruah, Asma A. Alothman, and Saikh Mohammad

Cite This: *ACS Omega* 2024, 9, 9147−9160

Read Online

ACCESS | Metrics & More | Article Recommendations

ABSTRACT: In this study, lead-free BiM^{2+}(Zn, Ca, Mg)Ti−$BiFeO_3$ ceramics are fabricated under eco-friendly hydrothermal reaction conditions at 250 °C. XRD patterns show that all the synthesized compounds exhibit a phase coexistence of monoclinic and tetragonal perovskite-type structures with a morphotropic phase boundary at x = 0.4, with minimum impurity. The calculated average crystallite/grain size of the samples was close to 50 nm at full width at half-maximum of the main peak. The corresponding bonds of the constituent elements were observed by FTIR analysis, which further supports the formation of the local structure. EDS analyses detect all of the elements, their quantities, and compositional homogeneity. SEM data show agglomerated and nearly spherical morphology with an average particle size of about 128 nm. All synthesized ceramic powders revealed thermal stability with trivial mass loss up to investigated high temperatures (1000 °C). The dielectric constant reached its maximum at 38.7 MHz and finally remained constant after 80 MHz for all nanoceramics. Because of the complementary impact of different compositions, the most effective piezoelectric characteristics of d_{33} = 136 pCN^{-1}, P_r = 8.6 pCN^{-1} cm^{-2}, and k_p = 11% at 30 °C were attained at x = 0.4 content for 0.4BiCaTi−0.6$BiFeO_3$ ceramic. The measured magnetic hysteresis data (M−H curve) showed a weak ferromagnetic nature with the highest moment of ∼0.23 emu/g for 0.4BiCaTi−0.6$BiFeO_3$, and other samples exhibited negligible ferromagnetic to diamagnetic transition. The optical response study shows that the 0.4BiMgTi−0.6$BiFeO_3$ sample yielded the maximal transmittance (50%), whereas the 0.4BiCaTi−0.6$BiFeO_3$ compound exhibited the highest refractive index. The calculated large band gap shows a high insulating or dielectric nature. Our findings demonstrate that the BiM^{2+}Ti−$BiFeO_3$ system, which was fabricated using a low-temperature hydrothermal technique, is an excellent lead-free piezoelectric and multiferroic nanoceramic.

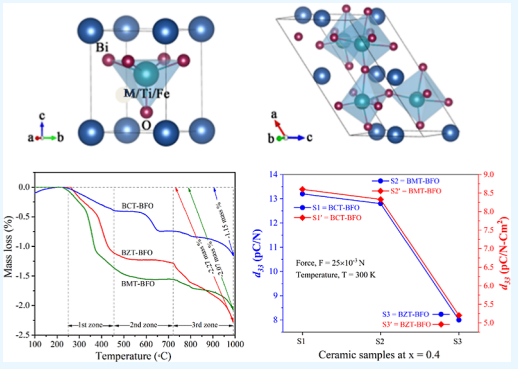

1. INTRODUCTION

Because of the growing knowledge of lead's environmental toxicity,[1−6] lead-free ferro/piezoelectrics have gained more and more interest. Due to increasing ecological worries, lead-free ferroelectric materials have experienced significant strides in recent years. The majority of the lead-free materials currently on the market are based on the perovskite complexes of $BaTiO_3$, $Bi_{0.5}Na_{0.5}TiO_3$, $K_{0.5}Na_{0.5}NbO_3$, and their corresponding configurations.[7] New lead-free materials are demanded to eliminate the barrier of unsatisfied properties such as a low Curie temperature (T_c) in $BaTiO_3$ or a low depolarization temperature (T_d) in $Bi_{0.5}Na_{0.5}TiO_3$. Importantly, chemical substitutions for both $PbTiO_3$ (PT) and $Bi(Zn_{0.5}Ti_{0.5})O_3$ (BZT), such as in PT−$Bi(Mg_{0.5}Ti_{0.5})O_3$, PT−$Bi(Ni_{0.5}Ti_{0.5})O_3$, BZT−$BaTiO_3$, BZT−$(Bi_{1/2}Sr_{1/2})(Zn_{1/2}Nb_{1/2})O_3$, and Bi-$(Zn_{0.5}Ti_{0.3}Mn_{0.2})O_3$ lead to change in c/a (lattice parameter) that significantly affect the T_c, polarization, and other properties of the products.[8−12] Furthermore, some novel properties are observed in Bi/Ti-based compounds, such as strong polarity in BZT, a good photovoltaic effect in PT−$Bi(Ni_{2/3}Nb_{1/3})O_3$, and multiferroicity in $BiFeO_3$, $NiTiO_3$, $MgTiO_3$, $BiFeO_3$, $CrBiO_3$, $ZnTiO_3$, $PbVO_3$, $BiMnO_3$, $BiCoO_3$, and $BiMnO_3$.[13−15] Furthermore, optical, light absorption,[16] and magneto-electronic attributes are very crucial to determining either semiconducting or insulating, as well as dielectric/piezoelectric properties for advanced applications in this field.[17,18] Subsequently, the precursor dynamics and their related physical properties of ABO_3-type ferroelectric have

Received: October 15, 2023
Revised: December 22, 2023
Accepted: January 24, 2024
Published: February 19, 2024

been investigated by inelastic light scattering.[19−21] Recently, double-perovskite Bi oxides are a new series of magnetic materials showing superconductivity; among them the novel A-site ordered double-perovskite[22−26] and simple perovskite[27,28] bismuthates have been reported. These substances were created hydrothermally at a low temperature,[29] which is likely to have encouraged the development of a structured framework.

In recent times, a new bismuth-based lead-free perovskite $(1 - x)Bi(Zn_{0.5}Ti_{0.5})O_3{-}xBiFeO_3$ (BZT−BF) has been synthesized via a high temperature and high pressure (HTHP) method, which exhibits giant polarization and possesses monoclinic and tetragonal phases with a morphotropic phase boundary (MPB) of monoclinic and tetragonal phases[30] at x = 0.5. The compound $(1 - x)$BZT−$x$$BFO_3$ exhibits a giant ferroelectric polarization ∼110 $\mu C/cm^2$, which is much higher than simple perovskites of PT (59 $\mu C/cm^2$)[31] and $BiFeO_3$ (60 $\mu C/cm^2$) [50], MPB systems of $PbZr_{0.52}Ti_{0.48}O_3$ (54 $\mu C/cm^2$) and PT−$BiScO_3$ (40 $\mu C/cm^2$),[32,33] or lead-free systems of $Bi_{0.5}Na_{0.5}TiO_3{-}BaTiO_3$ (41 $\mu C/cm^2$) and $K_{0.5}Na_{0.5}NbO_3$ (20 $\mu C/cm^2$).[34,35] However, these perovskite materials exhibit ferromagnetic, ferroelectric, and magneto-ferroelectric behavior, demonstrating multiferroic functionality. Of these, $BiFeO_3$ has gathered increasing interest as a promising high-temperature multiferroic and/or piezoelectric material, possessing a high Curie temperature T_c.[17,36] Moreover, optical absorbance, band gap, photocatalytic performance, and thermal stability of pure $BiFeO_3$ perovskite have been studied for potent application as a photocatalyst for the degradation of materials in the visible region.[37] Subsequently, it was discovered that the $BiFeO_3$ nanopowders had a single-phase perovskite configuration and were strongly crystalline.[17] It ought to be emphasized that the B-site replacement components synthesized from bismuth ferrite by the conventional approach belong to the identical space group, $R3c$ or Cc, as the parent $BiFeO_3$, even if distinct structural phases might develop during high-pressure synthesizing. Conversion polymorphism, a common occurrence in a high-pressure environment, was shown to be the cause of the observed result. Therefore, a thorough analysis of the structure, dielectric nature, and magnetic behavior of the as-prepared and switched polymorphism of the $(1 - y)BiFeO_{3-y}BiScO_3$ perovskites has been conducted.[38−40] Additionally, $BiFeO_3$ solid forms developed in conjunction with additional ABO_3-type perovskites, including $NaNbO_3$, $BaTiO_3$, $CaTiO_3$, $SrTiO_3$, and $Bi_{0.5}Na_{0.5}TiO_3$.[41] One of the systems that is investigated most extensively is $BiFeO_3{-}BaTiO_3$ (BF−BT).[42] In addition, moving the phase boundary (PB) closer to ambient temperature, creating a novel PB by doped ions or other elements, or creating patterned ceramics, having piezoelectric properties have undergone an important advancement.[43] ABO_3 compounds consisting of Zr^{4+}, Hf^{4+}, and Bi^{3+} have been discovered to significantly enhance the response of the piezoelectric by forming distinct PBs.[43,44] The previously discussed piezoelectric or ferroelectric materials are often created through a challenging experimental setup with restrictive conditions. Researchers have spent a lot of time and energy in recent years developing novel functioning ferroelectric and multiferroic compounds as well as refining processes for producing already existing goods. Typically, solid−state reactions (SSRs) and complex HTHP techniques are used to produce a majority of ferroelectric and multiferroic materials. On the contrary, a practical option might be applied to the hydrothermal process, which has developed into an innovative approach to the fabrication of multifunctional novel nanomaterials.

Moreover, ferroelectrics and multiferroics are important groups of multifunctional ceramics that are used in many electronic and electro-optic devices. For this reason, BM^{2+}(Zn, Ca, Mg, Ba, Sr)T−BFO system/compounds are strong candidates that can make miniature evolution in the magneto-electronic and/or spintronic sectors. So, this system might be a potential candidate for application in optical waveguides, frequency multipliers, holographic memory devices, and so on. In order to better understand the interaction between phase, microstructure, optical, thermal, magnetic, piezo, and dielectric characteristics of these ceramic frameworks, a new BM^{2+}(M = Zn, Mg, Ca)−BFO ferro/piezoceramic and multiferroic scheme was created. To the best of our knowledge, the divalent cations that are being substituted have not been subjected to the structural, morphological, elemental, optical, and magneto-electronic data that were acquired during the hydrothermal synthesis and characterization of a substantial amount of the $BiFeO_3$ dope perovskite series. Investigations into the differences in the physio-chemical and structural properties of isomorphous replacements are required in order to better understand the interesting features and predict the properties of novel constituents. In order to accomplish the innovative superior characteristics, the monoclinic/rhombohedral to tetragonal PB at x = 0.4 was constructed by substituting three distinct elements, which boosted the magnetic behavior, ferro/piezoelectric response, dielectric, optical, and thermal behaviors. Therefore, in the present research scheme, our main goal is to fabricate a BM^{2+}(Zn, Ca, Mg, Ba, Sr)T−BFO lead-free system of polycrystals or powders by incorporating various divalent elements via a ecofriendly low-temperature hydrothermal technique. Additionally, the multiferroic characteristics and compositional behaviors of the crystal structure are compared to those of the corresponding $BiFeO_3$ dope perovskites adjacent to the parent bismuth ferrite. Since Bi has a lead-like $6S^2$ stereochemically active lone-pair electron structure, this could lead to substantial oxygen hybridization, resulting in significant polarization and high T_c.[23] As a result, in our suggested material system, new characteristics like intense polarity and prospective high piezo/ferroelectricity and multifunctional attributes are anticipated.

Additionally, this study is notable for the following crucial factors related to the fabrication method. (1) Because the hydrothermal approach uses a low temperature, it may conserve energy and cost that are often associated with product creation expenses. (2) The hydrothermal method and the anticipated results are nontoxic and beneficial to the environment in contrast to other sophisticated synthesis techniques. (3) The quality of piezo and/or ferroelectric materials for energy storage device applications may be greatly improved by low-energy hydrothermal techniques.

2. EXPERIMENTAL SECTION

2.1. Sample Preparation. The employed hydrothermal approach eliminates the need for high-temperature requisitions, which helps the final crystals or powders avoid reclustering and contamination. In comparison to other processes, the hydrothermal approach offers a few additional benefits, including the lack of high-temperature conditions, which saves money and energy, and the ease with which the purity, size, and crystal form of the end products can be

https://doi.org/10.1021/acsomega.3c08072
ACS Omega 2024, 9, 9147−9160

controlled using basic equipment. Additionally, it is ideal for the formation of large-quality crystals and has the capacity to produce crystalline phases as well.[45] The starting materials Bi_2O_3, ZnO, CaO, MgO, TiO_2, and Fe_2O_3 with >99% purity are primarily selected for the present research project. All these high-quality raw ingredients were purchased from Sigma-Aldrich chemical sciences company to synthesize the final nanoceramic products. The expression that follows is used to retain the stoichiometric chemical composition for the constructed system: $Bi_2O_3 + 0.3(ZnO/CaO/MgO) + 0.5TiO_2 + 0.2Fe_3O_3 \rightarrow x[(Zn/Ca/Mg)_{0.5}, (Ti_{0.5})O_3-(1-x)BiFeO_3$, where $x = 0.4$.

The compounds were synthesized via a hydrothermal reaction in a Teflon-lined stainless steel autoclave with a capacity of about 70 mL. The initial ingredients were accurately weighed at different molar ratios and were maintained in an autoclave lined with Teflon that would dissolve them in the proper aqueous solution. The autoclave was then shut tightly to withstand the pressure and heat generated inside it. The hydrothermal reaction was then finished in the autoclaves by placing them in a heating oven for 48 h at a temperature of 250 °C. The autoclave was removed from the oven after the specified amount of reaction time to cool and depressurize in a water bath. The final precipitate was filtered, separated by deionized water washings, and dried in air at 70 °C for further characterization. Additionally, the items were ground into useable and finer ceramic powders using a mortar and pestle.

2.2. Characterizations. Characterization of the prepared samples is the most important part of evaluating their structure and physio-chemical properties. A number of techniques are used for the characterization of materials and studying their interesting characteristics. The specific characterization methods include powder X-ray diffraction (XRD) analysis, scanning electron microscopy-energy dispersive spectroscopy (SEM-EDS) analyses, Fourier transform infrared (FTIR), thermogravimetric analysis (TGA), ultraviolet−visible (UV) spectroscopy, vibrating sample magnetometer (VSM), piezoelectric testing, and dielectric/impedance spectroscopy. In the midst of these techniques, the phases of the products were examined by XRD powder (Rigaku, Ultima IV, Japan) pattern using CuK_α radiation of wavelength 1.5406 Å from a 2θ angle of 5 to 50° with a step mode of 0.2/min. The surface morphology, particle size, and elemental data and mapping of the hydrothermally prepared samples were investigated by employing a high-resolution electron microscope (Model CarlZEISS EVO, Germany) having a ×100,000 magnification scale operated at 30 V and an EDS X-ray Micro Analysis System (EDAX Inc., USA), respectively. Crystallite size, crystallinity, microstrain, and average particle sizes were estimated using the Debye−Scherer's formula and ImageJ software, respectively. TGA was used to assess thermal stability as an aluminum reference at an elevation rate of 10 °C min^{-1} through the ambient temperature to 1000 °C (PerkinElmer Simultaneous Thermal Analyzer STA 8000) using ∼10 mg samples. The optical absorbance and band gap of each sample were calculated by a UV spectrophotometer (Shimadzu, UV-2600i) in the range of 200−800 nm wavelength utilizing distilled water as solvent. The frequency-dependent dielectric constant and impedance analysis of each sample was performed by an LCR meter (Hioki LCR, Model-3535, Japan) and impedance spectrophotometer in the frequency range of 20 Hz to 70 MHz with an oscillating voltage of 500 mV at room temperature. Room-temperature field-dependent magnetic properties (hysteresis loop) of the fabricated samples were carried out using a VSM (Model DXV-100, China) up to 10 kOe magnetic field. Piezoelectric properties (d_{33} constant) of the fabricated ceramics were investigated at room temperature using a piezoelectric meter (model YE2730A, Sinocera, China) at a constant force of 25×10^{-3} N.

3. RESULTS AND DISCUSSION

3.1. Structural Analysis. The XRD patterns of hydrothermally synthesized $(1-x)BM^{2+}(Zn, Ca, Mg)T-xBFO$ ceramic compounds at $x = 0.4$ are shown in Figure 1. It is seen

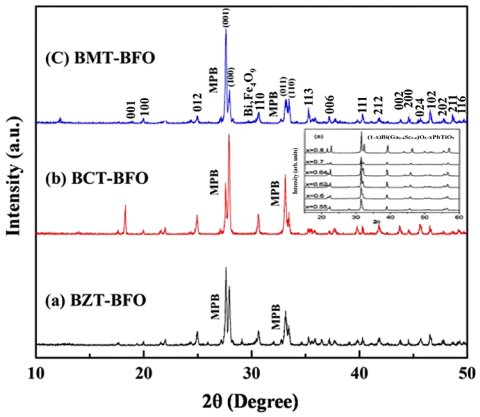

Figure 1. XRD patterns of (a) 0.4BZT−0.6BFO, (b) 0.4BCT−0.6BFO, and (c) 0.4BMT−0.6BFO ceramics at $x = 0.4$ composition.

that a continuous solid solution of the $BM^{2+}(Zn, Ca, Mg)T-BFO$ system with a perovskite structure with minimum impurities is obtained by a relatively low temperature (at 250 °C) hydrothermal method. The XRD patterns exhibit a phase coexistence of monoclinic or rhombohedral (space group: *Cc* or *R*3*c*) and tetragonal (space group *P*4*mm*) perovskite-type structures having lattice parameters, $a = 9.741(3)$ Å, $b = 5.694(1)$ Å, $c = 5.6701(6)$ Å for monoclinic or rhombohedral, and $a = b = 3.833$ Å, $c = 4.685$ Å for tetragonal phases with MPB at $x = 0.4$. Furthermore, JCPDS Card no. 81-2205 also fitting with peaks like those of the parent $BiZn_{0.5}Ti_{0.5}O_3$ perovskite has been attributed to the tetragonal perovskite phase.[46] Whereas, the XRD peaks and JCPDS card no. 86-1518 match up nicely with the perovskite distorted rhombohedral $BiFeO_3$ structure[17] or monoclinic phase[30,38] in $BiFe_{1-y}[Zn_{0.5}Ti_{0.5}]yO_3$. Most of the corresponding peaks are indexed for both phases with the least impurity, and MPBs are visualized at $x = 0.4$. It is widely recognized that the majority of MPBs exhibit highly overlapped peaks in the two phases.[32,34] Therefore, the true structure data associated with MPBs with highly overlapping peaks are hard to uncover. Importantly, the phase of the synthesized system is also identical to the reported $(1-x)Bi(Zn_{0.5}Ti_{0.5})O_3-xBiFeO_3$ system[18,30,47] prepared by the HTHP method and SSRs. In the present scheme, we replace M with various divalent transition metals such as Zn, Ca, and Mg to obtain a similar phase by an eco-friendly low-temperature hydrothermal reaction.

It is also observed from Figure 1 that there are splits in the peak observed at 2θ of about 27 and 33°, which are very similar to $(1-x)Bi(Mg_{1/2}Ti_{1/2})O_3-xPbTiO_3$,[8] $(1-x)Bi(Ga_{1/4}Sc_{3/4})O_3-xPbTiO_3$[48] (shown in the inset), $(1-x)(Bi_{1-y}Li_y)$, and $(1-x)(Sc_{1-y}Sb_y)O_3-xPbTiO_3$[49] com-

https://doi.org/10.1021/acsomega.3c08072
ACS Omega 2024, 9, 9147−9160

pounds, indicating the coexistence of tetragonal and rhombohedral or monoclinic (because the peak at 23° shifts to 27°) phases of BM^{2+}(Zn, Ca, Mg)T−BFO. It is indicated that the MPB composition is located at x = 0.4 for all compounds in this study. Among these synthesized samples, the BMT−BFO ceramic compound exhibits a nearly pure MPB composition with minimum impurities (Figure 1c).

The corresponding crystal structure of the prepared BM^{2+}(Zn, Ca, Mg)T−BFO compounds is shown in Figure 2

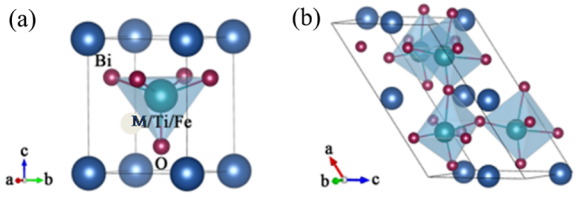

Figure 2. Crystal structures of the (a) tetragonal and (b) monoclinic phases of $(1-x)BM^{2+}$(Zn, Ca, and Mg)T−xBFO compounds at x = 0.4 synthesized at 250 °C.

drawn by VESTA software.[50] In the tetragonal structure, the Bi atom is located at the corner (A site) and Zn/Ca/Mg, Ti, and Fe atoms are located at the center (B site). A network of corner-sharing BiO_6 octahedra with oxygen atoms is at the corner of the octahedra (Figure 2a).

With the chemical substitution, these compounds may transform from the tetragonal phase (Figure 2a) to mixed phases of tetragonal and monoclinic (or rhombohedral), as seen in the XRD pattern. The large tetragonal distortion leads to pyramidal coordination in the monoclinic or rhombohedral phase (Figure 2b) rather than octahedral coordination in the tetragonal phase. In addition, it is indicated that the MPB composition at x = 0.4 is located along the (001) plane for all compounds. Utilizing the Debye−Scherrer's formula,[51] the average particle size of the BM^{2+}T−BFO powder was calculated using X-ray line width as follows (eq 1)

$$D = \frac{K\lambda}{\beta \cos\theta} \tag{1}$$

where D = particle diameter (Å), λ = wavelength of the radiation (for the study, it is equal to 0.154 Å), θ = Bragg's angle (deg), and β = full width at half-maximum. The porosity (P) of the prepared ceramics[52] is also calculated by the following expression (eq 2)

$$P = \frac{\rho\mathrm{XRD} - \rho\mathrm{cal}}{\rho\mathrm{XRD}} \times 100 \tag{2}$$

The calculated average crystallite size, microstrain, porosity, and crystallinity of the synthesized samples are summarized in Table 1. We see that the lowest crystallite size (43.76 nm) than others is observed for the sample BZT−BFO at x = 0.4 composition. This scenario might be due to higher crystalline deformation than other materials, which can be seen.[53] The porosity of the samples, which is opposite of the solidity, was on the scale of 24 to 28%, whereas the ceramic powder BMT−BFO showed the minimum porosity (24%).

3.2. Morphological and Elemental Analyses. The measured surface morphology and particle size of the four synthesized samples are displayed in Figure 3. All of the prepared powder samples were dominantly agglomerated, while the sample BZT−BFO in Figure 3a showed the lowest agglomeration. On the other hand, particles of the powder samples/compositions BCT−BFO and BMT−BFO in Figure 3b,c, respectively, are well-resolved and distinctive in nature. Furthermore, the particles are almost circular in shape and somewhat uniform, especially for the samples Figure 3a,c, which might be due to the presence of different compositions in the samples. The average particle size in the fabricated samples was approximately 180, 228, and 128 nm, respectively, for the BZT−BFO, BCT−BFO, and BMT−BFO ceramics, which has been determined by using ImageJ software.[54]

Moreover, EDS spectra, quantitative data, elemental homogeneity, and mappings of the synthesized samples were collected and are shown in Figures 4−6. EDS spectra of the 0.4BiZnTi−0.6BiFeO ceramic confirm the presence of all corresponding elements with dominating Bi peak and quantity, which is displayed in the inset table of Figure 4a. In addition, an almost homogeneous distribution of all elements was seen from the EDS mapping images of Figure 4b for the material. Similarly, the other two ceramics 0.4BiCaTi−0.6BiFeO and 0.4BiMgTi−0.6BiFeO also ensure the existence of all elements in the spectra, quantity, and elemental mapping (homogeneity) in Figures 5a,b and 6a,b, respectively.

3.3. FTIR Spectroscopic Analysis. To identify each specific chemical bond, FT-IR spectra of $0.4BM^{2+}T-0.6BFO$ (M = Zn, Ca, or Mg) compounds were measured using a PerkinElmer Spectrum 100 FT-IR spectrometer, as shown in Figure 7. It is well-known that the bands between 700 and 400 cm^{-1} are mainly attributed to the formation of metal oxides. The formation of perovskite structure can be confirmed by the presence of a metal−oxygen band.[55] The peaks at around 540 and 460 cm^{-1} are assigned to the mode of stretching vibrations of Fe−O and bending vibration of Fe−O, respectively.[56] In addition, the bands observed at around 560 and 460 cm^{-1} in all compounds reveal the characteristic vibrations of the Bi−O bond.[57] Wang et al. also reported the Bi−O stretching vibrations at 515 cm^{-1}.[58] Moreover, the peak at 460 cm^{-1} in BZT-BFO may also be attributed to the stretching vibrations of Zn−O bonds.[59] In BCT−BFO, the band at around 538 cm^{-1} corresponds to the Ca−O bonds.[60] Furthermore, the peak at 539 cm^{-1} in the compound BMT−BFO confirmed the presence of Mg−O vibrations.[61,62] In the IR spectra of BM^{2+}T−BFO, the bands at around 3400 and 1628 cm^{-1} are correlated to stretching and bending vibrations of the OH

Table 1. Fabricated Materials' Average Crystallite Size, Microstrain, Crystallinity, Particle Size, Porosity, and Solidity were Estimated from the XRD and SEM Data

samples	from XRD	from SEM			
	average crystallite size (nm)	microstrain	crystallinity (%)	average particle size (nm)	solidity and porosity (%)
BZT−BFO	43.76	7.438×10^{-6}	61.38	167	0.73/27
BCT−BFO	49.66	5.495×10^{-6}	76.80	244	0.72/28
BMT−BFO	51.72	4.077×10^{-6}	56.10	128	0.76/24

https://doi.org/10.1021/acsomega.3c08072
ACS Omega 2024, 9, 9147−9160

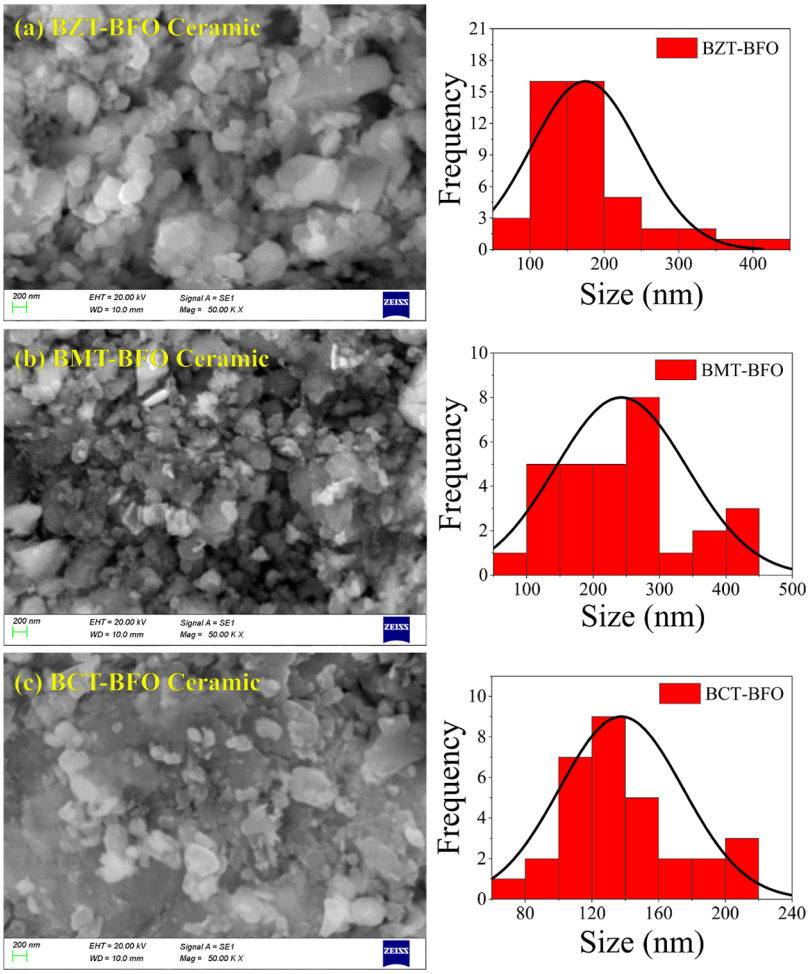

Figure 3. Surface morphology and particle size distribution of the hydrothermally prepared samples (a) BZT−BFO, (b) BMT−BFO, and (c) BCT−BFO at 250 °C.

bond, respectively, to confirm the presence of water molecules.[63] In BMT−BFO, sharp peaks at 3697 and 1384 cm^{-1} correspond to Mg−OH stretching vibration and bending vibration, respectively.[64] However, the peaks at 845 cm^{-1} for BZT−BFO and 865 cm^{-1} for BCT−BFO are assigned to the vibrational modes of Fe−O, Bi−O−Bi, and Bi−O−Fe stretching, which indicates the oxygen ion vibrations of oxygen octahedra in the structure,[65,66] whereas this peak is almost merged in the BMT−BFO system. Therefore, the detection of all corresponding bonds in the hydrothermally fabricated samples ensures high crystallinity and pure local structure formation.

3.4. Thermal Stability Analysis. To investigate the thermal stability of the hydrothermally synthesized products of $0.4BM^{2+}T-0.6BFO$ (M = Zn, Ca, Mg), we carried out TGA using a PerkinElmer Simultaneous Thermal Analyzer STA 8000 with a heating rate of 10 °C min^{-1} within a temperature range 100−1000 °C, as shown in (Figure 8). There are no significant mass losses below 250 °C, which means that the compounds are stable up to a 250 °C temperature. Three major thermal changes are visualized in Figure 8, where the first change is observed after 250 °C. The loss of weight at temperatures higher than 200 °C mainly comes from the crystallization of water.[64] The second thermal change occurred at around 455 and 650 °C, possibly corresponding to the formation of the metal oxide phase of $BiFeO_3$.[37,67] The third alteration occurs after 650 °C as a result of the bismuth oxide phase shifting and moving from a ferrous to a ferric higher oxidation state.[37] At 720 °C, the α phase of bismuth oxide is converted to the δ phase[68] as well. The TG-curves exhibit total mass losses of 2.27, 1.15, and 2.07% for BZT-BFO, BCT-BFO, and BMT-BFO, respectively, up to around 1000 °C (Figure 8). It is interesting to note that these hydrothermally produced samples have far lower total masses and thermal disintegration than pure $BiFeO_3$ perovskite,[37] which suggests that the materials are thermally stable for the applications even at high temperatures.

3.5. Optical Properties. The optical properties of the 0.4BiZnTi−0.6BiFeO, 0.4BiCaTi−0.6BiFeO, and 0.4BiMgTi−0.6BiFeO samples have been studied using an UV spectrophotometer. Figure 9 shows the absorbance, transmittance, reflectance, and refractive index spectra of the prepared samples in the wavelength range from 200 to 800 nm. The absorption spectra for the aforementioned show that the absorption edges lie within the ultraviolet region with the highest or maximum absorption for the 0.4BCT−0.6BFO ceramic. The absorbance value of the samples dropped drastically in the UV region and remained almost linear in the visible range and up to 800 nm.

A very small peak of absorption has been identified, implying that these samples are UV−visible light transparent.[69]

https://doi.org/10.1021/acsomega.3c08072
ACS Omega 2024, 9, 9147−9160

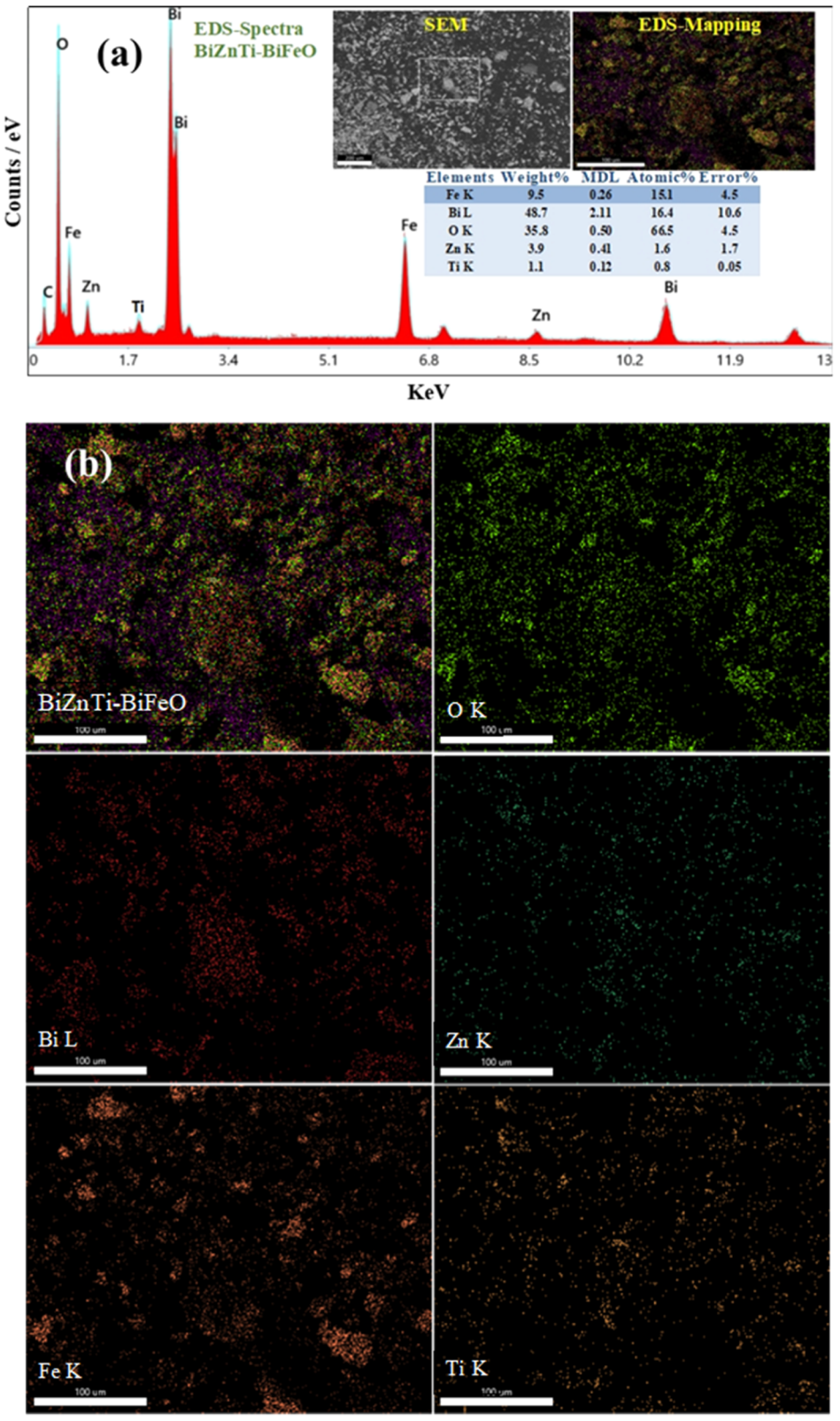

Figure 4. (a) EDS spectra and inset show the quantitative data table, SEM, and EDS mapping; and (b) elemental mapping of all atoms in $0.4BiZnTi-0.6BiFeO_3$ perovskite.

The absorption (A) and transmittance (T) of a sample are linked by the formula[70] (eq 3)

$$A = -\log 10(T) \quad (3)$$

The transmittance of BMT−BFO is more than 50% in the ultraviolet spectrum, while it is more than 45% for BZT−BFO and 20% for BCT−BFO in the same region, as shown in Figure 9b. At a visible wavelength, the transmittance spectrum of BMT−BFO is also more than that of BZT−BFO and BCT−

https://doi.org/10.1021/acsomega.3c08072
ACS Omega 2024, 9, 9147−9160

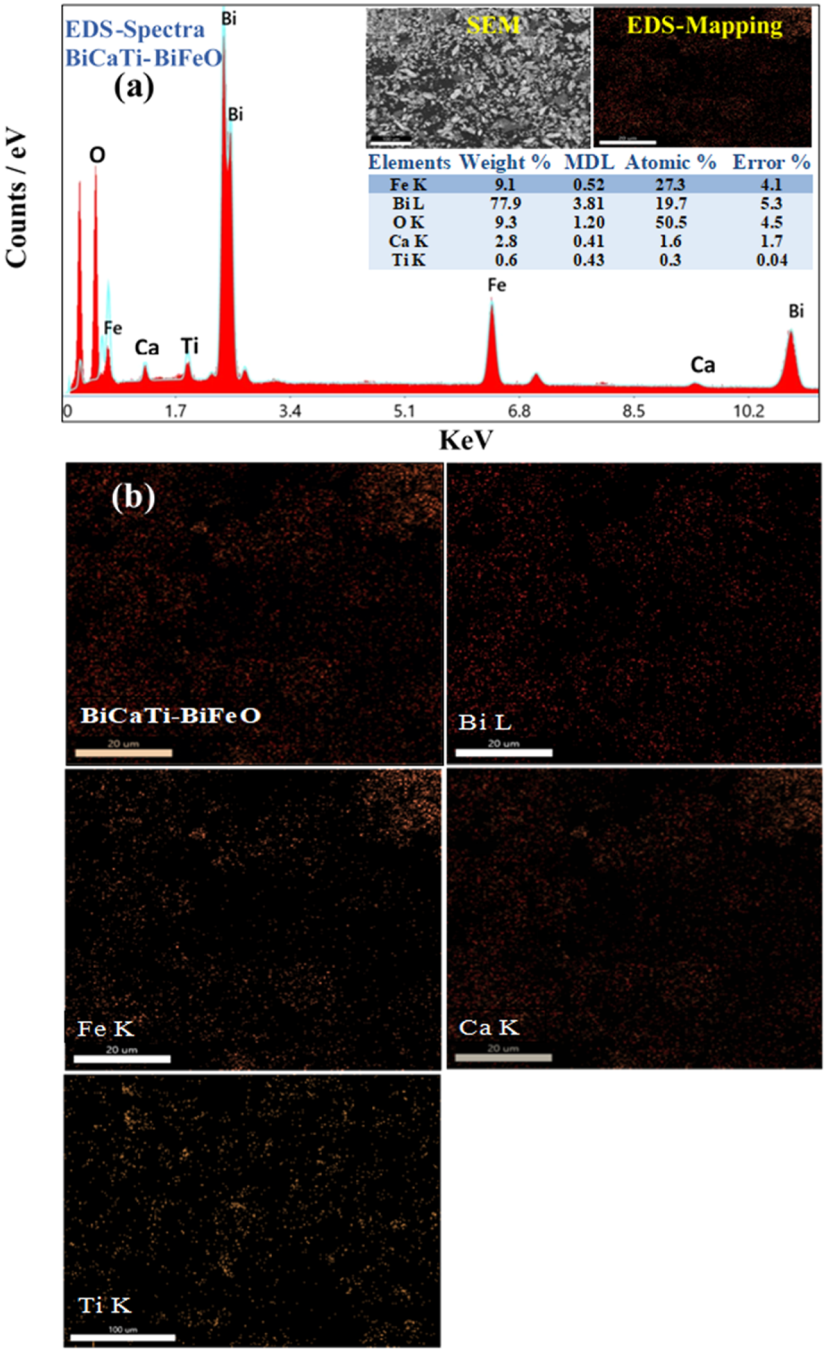

Figure 5. (a) EDS spectra and inset show the quantitative data table, SEM, and EDS mapping; and (b) elemental mapping of all atoms in $0.4BiCaTi{-}0.6BiFeO_3$ perovskite ceramic.

BFO due to its high optical band gap. The lower optical band gap is responsible for the lower transmittance of a material.[71−76] The reflectance of BMT−BFO, BCT−BFO, and BZT−BFO ceramics as a function of wavelength is illustrated in Figure 9c. BCT−BFO shows large reflectance and BZT−BFO shows less almost constant reflectance in the wavelength region of 200−800 nm.

The refractive index of the ceramics is calculated using the Fresnel formula[77,78] (eq 4)

$$n = \left(\frac{1+R}{1-R}\right) + \left[\frac{4R}{(1-R)^2} - K^2\right]^{1/2} \quad (4)$$

where R is the reflectance, and K is the excitation coefficient of the ceramics.

$K = (^{\alpha\lambda}/_{4\pi})$ where α is the optical absorption coefficient, and λ is the incident wavelength. The refractive index (n = 5.26) of BCT−BFO is much higher than that of BMT−BFO (n = 3.67) and BZT−BFO (n = 1.88) in the region 200−800 nm, as shown in Figure 9d. Notably, the refractive index shows slight rising trends in the visible range and remains nearly unchanged after 700 nm.

The energy density of states inside the optical band gap of the films has a direct relationship with the performance of these optical parameters.[77,78] The optical band gap is the threshold for photons to be absorbed, while the transport gap

https://doi.org/10.1021/acsomega.3c08072
ACS Omega 2024, 9, 9147−9160

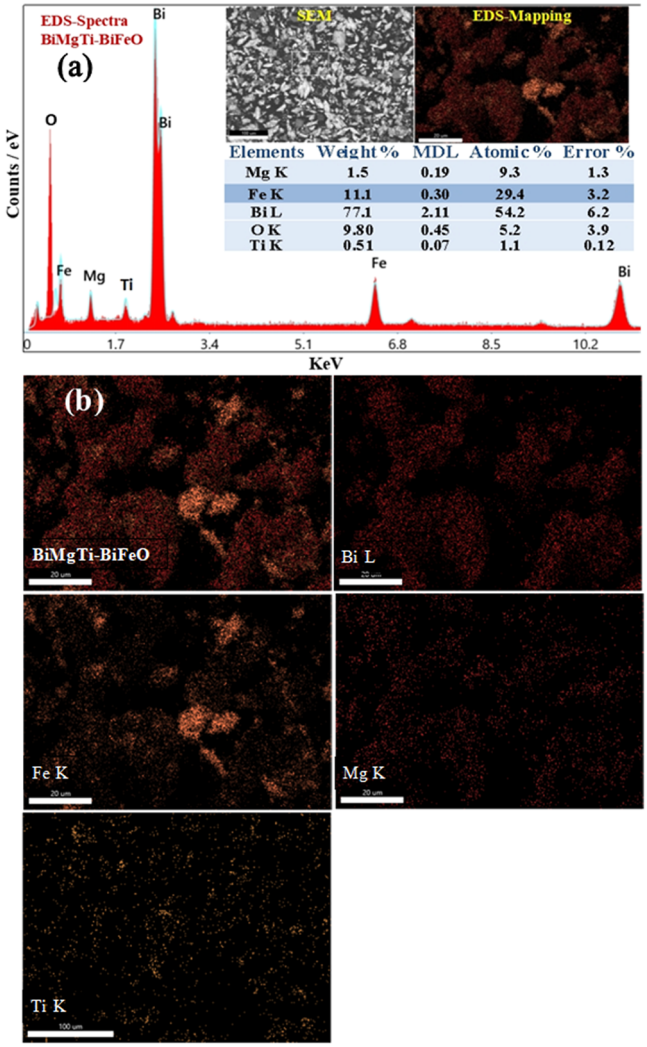

Figure 6. (a) EDS spectra and inset show the quantitative data table, SEM, and EDS mapping; and (b) elemental mapping of all atoms in 0.4BiMgTi−0.6BiFeO$_3$ functional ceramic.

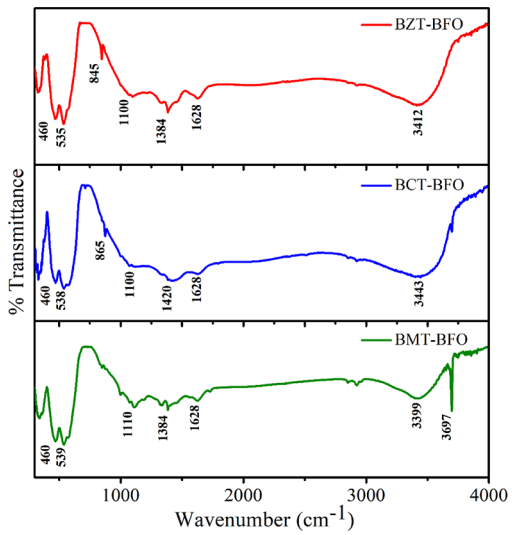

Figure 7. FTIR spectra of hydrothermally synthesized $(1-x)$BM^{2+}(Zn, Ca, and Mg)T−xBFO perovskite ceramics.

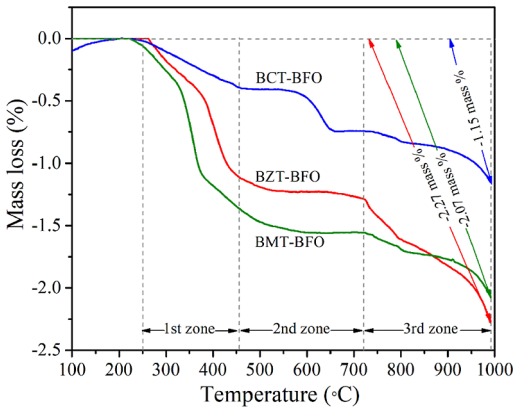

Figure 8. TGA graph and nature of hydrothermally prepared BM^{2+}T−BFO (M = Ca, Zn, and Mg) ceramic powders at 250 °C.

is the threshold for creating an electron−hole pair that is not bound together. The optical band gap is at a lower energy than the transport gap. The optical band gap is traditionally measured by extrapolating the photon energy along the *X*-axis and the linear region of the square of the product of the absorption coefficient and photon energy along the *Y*-axis, known as the Tauc plot. Tauc's relationship has been used to determine the energy band gap of the samples[78,79] (eq 5)

$$(\alpha h\nu) = A(h\nu - E_g)^n \quad (5)$$

where A is the transition probability-dependent factor. The index (n) is connected to the density of state distribution and is used to describe what kind of transition occurs. The value of n is 0.5 for direct allowed and 1.5 for direct forbidden transition, while n is 2 and 3 for indirect allowed and forbidden transitions, respectively.[69,70,77] As BFO-based samples have been investigated to allow direct transition, the index n has been set to 0.5 in this study, as illustrated in Figure 10a. The direct band gap energies for BZT−BFO, BCT−BFO, and BMT−BFO samples have been calculated to be 5.78, 5.68, and 5.84 eV, respectively. Figure 10b shows the $(\alpha h\nu)^{1/2}$ versus E (eV) curve for all ceramics. To accomplish the indirect transition, the index n has been fixed to 2. The indirect band gap energies for BZT−BFO, BCT−BFO, and BMT−BFO samples have been determined to be 5.32, 5.13, and 5.71 eV, respectively. These large band gaps are responsible for the successive decrease of photocatalytic activity under ultraviolet light with increasing wavelength. The variation of the band gap is thought to be caused by the variation in photocatalytic activity. The photocatalytic activity of Zn, Ca, and Mg is different, so the band gap of the prepared samples of BZT−BFO, BCT−BFO, and BMT−BFO are also different.

3.6. Dielectric Properties. The dielectric constant is a multidimensional quantity with real and imaginary parts. The dielectric constant's real portion specifies how electrical energy is stored as potential energy in a dielectric substance by polarizing it. The dielectric loss is expressed by the dielectric constant's imaginary portion.[80]

Dielectric loss is the loss of electromagnetic energy propagating inside a dielectric. It usually happens for two reasons. One is the relaxation effect; basically, the oscillating electric field polarizes the dielectric, and this creates a dipole that is also oscillating; this dipole absorbs and then rescatters the electric field. Of course, this response is not instantaneous; the dipole's response is always delayed by some phase with

https://doi.org/10.1021/acsomega.3c08072
ACS Omega 2024, 9, 9147−9160

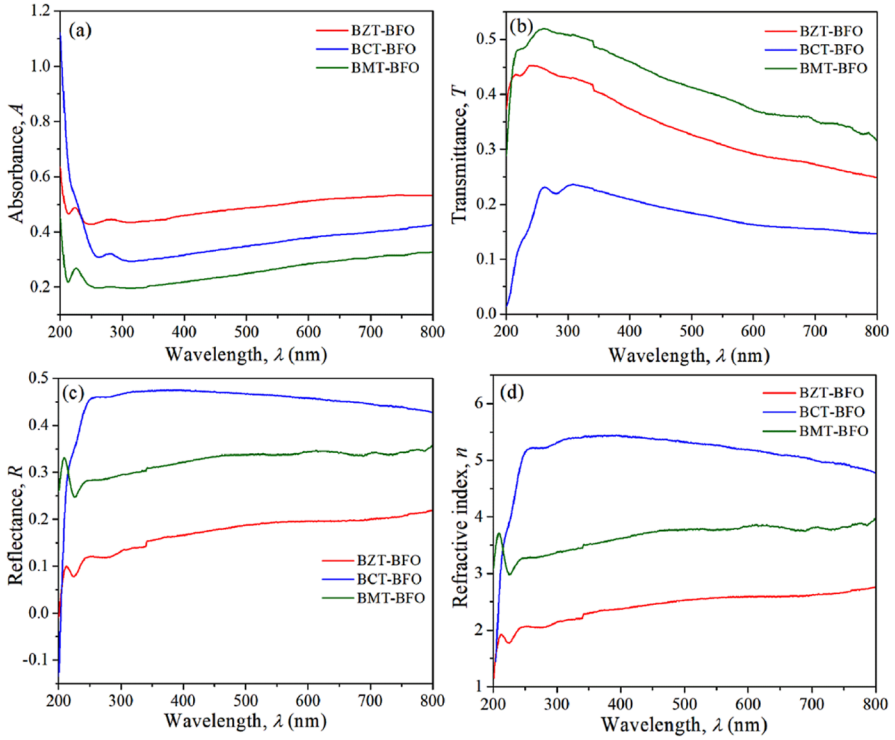

Figure 9. Optical data and UV−vis absorption spectra for BZT−BFO, BCT−BFO, and BMT−BFO ceramic compounds.

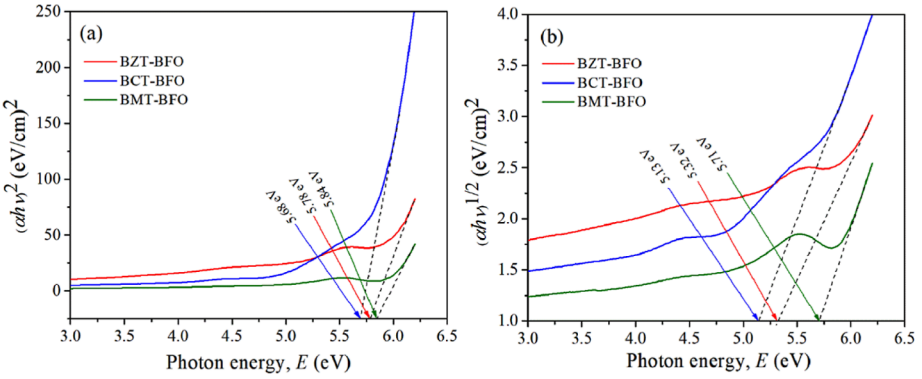

Figure 10. Tauc plot for estimation of the direct and indirect band gaps for BZT−BFO, BCT−BFO, and BMT−BFO ceramic compounds.

respect to the field. The second reason is resonance; when the electric field's frequency resonates with the electronic, vibrational, and rotational transitions of the dielectric, the dielectric will absorb the energy in order to perform such transition, and the energy will dissipate.

The dielectric loss of the prepared samples was measured by a precision impedance analyzer. The frequency dependence dielectric constant as well as dielectric loss of all samples has been measured in the frequency range of 20 Hz to 70 MHz with the oscillating voltage of 500 mV at room temperature as demonstrated in Figure 11.

The following equations (eqs 6 and 7) have been used to get the dielectric constant ε' and dielectric loss factor $(\tan \delta)$.[81]

$$\varepsilon' = \left(\frac{Cd}{\varepsilon_0 A}\right) \tag{6}$$

$$\tan \delta = \frac{\varepsilon'}{\varepsilon''} \tag{7}$$

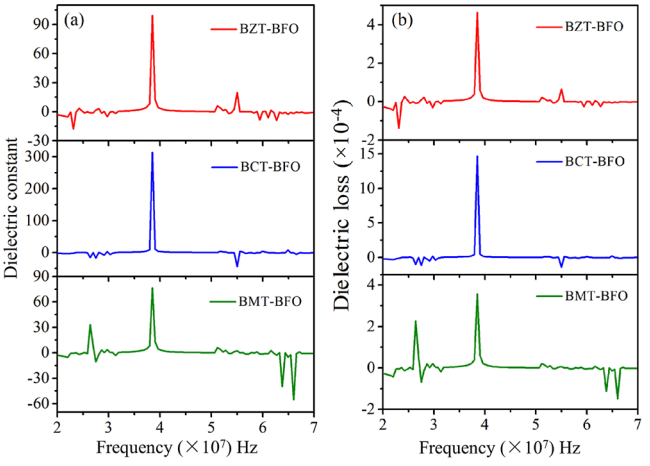

Figure 11. (a) Dielectric constant and (b) dielectric loss of BZT−BFO, BCT−BFO, and BMT−BFO ceramic compounds as a function of frequency.

https://doi.org/10.1021/acsomega.3c08072
ACS Omega 2024, 9, 9147−9160

where C is the capacitance, A is the area of the electrode, ε_0 is the permittivity in free space, d is the thickness, ε is the real part, and ε'' is the imaginary part of the dielectric constant of the samples.

Due to the probable interfacial or space charge polarization phenomena, both the dielectric constant and dielectric loss factor show an identical tendency of reducing value with increasing frequency. The dielectric constant and loss reached a maximum value around a frequency of 38.6 MHz. The dielectric constant values were found to be approximately 315, 100, and 80 for 0.4BCT−0.6BFO, 0.4BZT−0.6BFO, and 0.4BMT−0.6BFO ceramics, respectively. The highest dielectric constant value for BCT−BFO has been noticed in this investigation compared to the other two samples (BZT−BFO and BMT−BFO). We conclude that BCT−BFO has larger charges, as well as a significant number of grain boundaries. As a result, it shows a larger dielectric constant value at a lower frequency.[82] All samples display lower values of dielectric constant at higher frequencies due to the low space-charge polarization. Furthermore, the Maxwell−Wanger interfacial-type polarization might be used to describe the dramatic fall of the dielectric constant at higher frequencies.[83]

The real part of the dielectric constant, as well as the loss factor, are inversely proportional to frequency, according to Maxwell−Wanger theorem.[84] It has been seen that the loss tangent of all samples is relatively high in the lower region, in comparison with the higher frequency region. Due to the inhibiting of the domain wall, the dielectric loss is low at higher frequencies.[80] The dielectric loss factor is also affected by a number of parameters, including sample stoichiometry, structural homogeneity, sintering temperature, and so on.[85]

3.7. Piezoelectric Measurements. The $(1-x)BM^{2+}T-xBFO$ ceramics' piezoelectric constant, d_{33}, at $x = 0.4$ composition in the room temperature is shown in Figure 12.

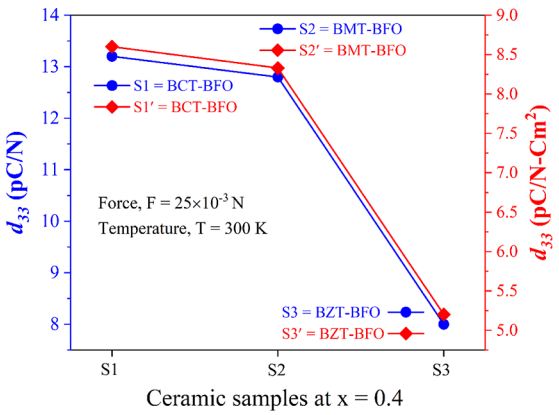

Figure 12. Change of the $BM^{2+}T-BFO$ (M = Ca, Mg, and Zn) ceramics' piezoelectric constant (d_{33}) and remnant polarization (P_r) under a constant force of 25×10^{-3} N at ambient temperature.

It is seen that for the BCT−BFO ceramic the value of d_{33} reached a maximum value of 136 pC/N for $x = 0.4$. Whereas the ceramic powder BMT−BFO at the same composition exhibited a slightly lower value of piezoelectric constant, and a significantly lower value of that was found for the sample BZT−BFO at the same $x = 0.4$. Furthermore, the estimated residual polarization (P_r) in the pC/NCm^2 unit (Figure 12 right scale) also changed following the analogous trend of the piezo constant. Because of M/R-T phase coexistence, more contributing polarization states might occur even at room temperature, which leads to the higher d_{33} by polarization rotation.[53] However, the fundamental lattice variance as well as external (domain flipping and phase border moves) effects with increased temperature are responsible for the net enhancement of piezoelectric characteristics, which results in a rise in piezoelectric characteristics. Thus, it is possible to achieve a better d_{33} value and other electronic attributes of our synthesized ceramics as a function of temperature durability[18,30] for future energy storage applications.

3.8. Magnetic Properties by M−H Curves. Figure 13 displays the M−H hysteresis loop data of hydrothermally synthesized ceramics under room-temperature conditions. Among the three compounds, the 0.4BZT−0.6BFO ceramic shows moderate ferromagnetic behavior and a high coercive field of ∼0.9 kOe with the increment of magnetic field up to 9 kOe, and a slight diamagnetic transition (Figure 13a) is seen at about 2 kOe field. In Figure 13b, the compound 0.4BCT−0.6BFO reveals very weak ferromagnetism with remnant magnetic polarization (M_r) and a low coercive field of 0.012 emu/g and 0.161 kOe, respectively, and a giant diamagnetic transition at 7 kOe field occurs for the material. Moreover, the ceramic powder 0.4BMT−0.6BFO exhibits strong diamagnetism at a high magnetic field (9 kOe) and a weak ferromagnetic transition originates at zero magnetic field (H_{ext}) with a small coercive field and remnant polarization of 0.14 kOe and 0.014 emu/g, respectively. The coexistence of such ferromagnetic and diamagnetic states might be originated due to the presence of both magnetic and diamagnetic or nonmagnetic materials in the studied compounds and has been investigated in many materials already.[86−88]

4. CONCLUSIONS

$0.4BiM^{2+}(Zn, Ca, and Mg)Ti-0.6BiFeO_3$ ceramic specimens were synthesized in the current work using an ecologically friendly hydrothermal procedure at 250 °C. XRD results suggest the presence of a MPB with monoclinic or rhombohedral to tetragonal symmetry at $x = 0.4$ compositions and a mean grain size of around 50 nm. FE-SEM images show the predominately agglomerated nearly spherical morphology with particle sizes of 180, 228, and 128 nm, respectively, for the BZT−BFO, BCT−BFO, and BMT-BFO nanoceramics. EDS data confirmed the presence of Bi, Zn, Ca, Mg, Ti, Fe, and O atoms, both in spectra and quantity, with an almost homogeneous distribution. FTIR spectra detect the associated bonds of the constituent elements, such as Fe−O, Bi−O, Ti−O, Bi−O−Fe, etc., as well as the bonds of M^{2+} cations. All ceramic powders demonstrated thermal stability at high temperatures with minimal mass degradation. UV data show that the direct band gap energies for BZTBFO, BCTBFO, and BMTBFO were calculated to be 5.44 5.84, and 5.90 eV, respectively. The prepared samples' highest dielectric constant reached peak values of 100, 317.13, and 76.92 for BZT−BFO, BCT−BFO, and BMT−BFO at 38.7 MHz, respectively. It is evident that while the dielectric constant is minimal, the dielectric loss is the largest, particularly in low-frequency zones. Among the fabricated samples, the highest ferromagnetism of 0.23 emu/g was observed for the BCT−BFO ceramic and ferromagnetic to diamagnetic transformation originated for all materials. The most potent piezoelectric performances for BCT−BFO nanoceramics at $d_{33} = 136$ pCN^{-1}, $P_r = 8.6$ pC/NCm^2, $T = 25$ °C, and $k_p = 11\%$ were attained at $x = 0.4$. The research further suggests that the single-step hydrothermal

https://doi.org/10.1021/acsomega.3c08072
ACS Omega 2024, 9, 9147−9160

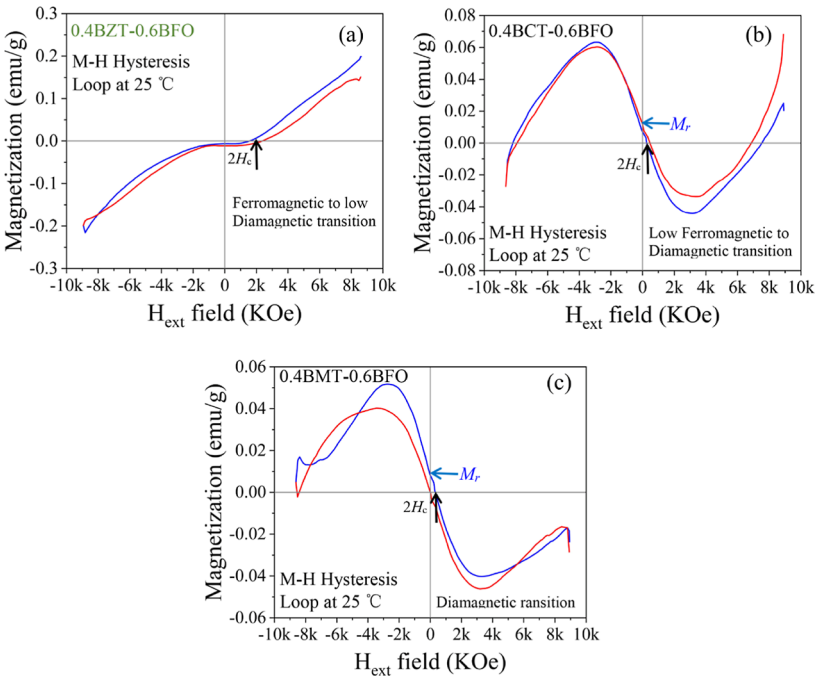

Figure 13. M−H hysteresis loop behavior of (a) 0.4BZT−0.6BFO, (b) 0.4BCT−0.6BFO, and (c) 0.4BMT−0.6BFO ceramic materials at room temperature.

process and the introduction of M^{2+} atoms are efficient to improve the magneto-electronic efficiency of lead-free $BiM^{2+}Ti-BiFeO_3$ piezo/ferroelectric and multiferroic ceramics.

■ ASSOCIATED CONTENT

Data Availability Statement

The raw/processed data required to reproduce these findings cannot be shared at this time as the data also forms part of an ongoing study.

■ AUTHOR INFORMATION

Corresponding Authors

M. H. Kabir Rubel − *Department of Materials Science and Engineering, University of Rajshahi, Rajshahi 6205, Bangladesh;* orcid.org/0000-0001-9420-4335; Email: mhk_mse@ru.ac.bd

M. Khalid Hossain − *Institute of Electronics, Atomic Energy Research Establishment, Bangladesh Atomic Energy Commission, Dhaka 1349, Bangladesh; Department of Advanced Energy Engineering Science, Interdisciplinary Graduate School of Engineering Sciences, Kyushu University, Fukuoka 816-8580, Japan;* orcid.org/0000-0003-4595-6367; Email: khalid.baec@gmail.com, khalid@kyudai.jp

Rajesh Haldhar − *School of Chemical Engineering, Yeungnam University, Gyeongsan 38541, Republic of Korea;* orcid.org/0000-0003-3120-6733; Email: rajeshhaldhar.lpu@gmail.com

Authors

K. Monower Hossain − *Department of Materials Science and Engineering, University of Rajshahi, Rajshahi 6205, Bangladesh*

G. F. Ishraque Toki − *College of Materials Science and Engineering, Donghua University, Shanghai 201620, China;* orcid.org/0000-0002-6761-3042

Latha Marasamy − *Facultad de Química, Materiales-Energía, Universidad Autónoma de Querétaro, Santiago de Querétaro, Querétaro C.P.76010, Mexico;* orcid.org/0000-0002-2564-0894

Md Hasan Ali − *Department of Electrical and Electronic Engineering, Begum Rokeya University, Rangpur 5400, Bangladesh*

Smriti Baruah − *Department of ECE, Madanapalle Institute of Technology & Science, Madanapalle 517325, India*

Asma A. Alothman − *Department of Chemistry, College of Science, King Saud University, Riyadh 11451, Saudi Arabia*

Saikh Mohammad − *Department of Chemistry, College of Science, King Saud University, Riyadh 11451, Saudi Arabia*

Complete contact information is available at: https://pubs.acs.org/10.1021/acsomega.3c08072

Notes

The authors declare no competing financial interest.

■ ACKNOWLEDGMENTS

This work was funded by the Researchers Supporting Project Number (RSP2024R243), King Saud University, Riyadh, Saudi Arabia.

■ REFERENCES

(1) Pandey, R.; Bhattarai, S.; Sharma, K.; Madan, J.; Al-Mousoi, A. K.; Mohammed, M. K. A.; Hossain, M. K. Halide Composition Engineered a Non-Toxic Perovskite-Silicon Tandem Solar Cell with 30.7% Conversion Efficiency. *ACS Appl. Electron. Mater.* **2023**, *5* (10), 5303−5315.

(2) Hossain, M. K.; Toki, G. F. I.; Kuddus, A.; Rubel, M. H. K.; Hossain, M. M.; Bencherif, H.; Rahman, M. F.; Islam, M. R.; Mushtaq, M. An Extensive Study on Multiple ETL and HTL Layers to Design and Simulation of High-Performance Lead-Free $CsSnCl_3$-Based Perovskite Solar Cells. *Sci. Rep.* **2023**, *13* (1), 2521.

(3) Hossain, M. K.; Chanda, R.; El-Denglawey, A.; Emrose, T.; Rahman, M. T.; Biswas, M. C.; Hashizume, K. Recent Progress in

https://doi.org/10.1021/acsomega.3c08072
ACS Omega 2024, 9, 9147−9160

Barium Zirconate Proton Conductors for Electrochemical Hydrogen Device Applications: A Review. *Ceram. Int.* **2021**, *47* (17), 23725−23748.
(4) Bencherif, H.; Khalid Hossain, M. Design and Numerical Investigation of Efficient $(FAPbI_3)_{1-x}(CsSnI_3)_x$ Perovskite Solar Cell with Optimized Performances. *Sol. Energy* **2022**, *248*, 137−148.
(5) Hossain, M. K.; Arnab, A. A.; Das, R. C.; Hossain, K. M.; Rubel, M. H. K.; Rahman, M. F.; Bencherif, H.; Emetere, M. E.; Mohammed, M. K. A.; Pandey, R. Combined DFT, SCAPS-1D, and WxAMPS Frameworks for Design Optimization of Efficient Cs_2BiAgI_6-Based Perovskite Solar Cells with Different Charge Transport Layers. *RSC Adv.* **2022**, *12* (54), 34850−34873.
(6) Hossain, M. K.; Rubel, M. H. K.; Toki, G. F. I.; Alam, I.; Rahman, M. F.; Bencherif, H. Effect of Various Electron and Hole Transport Layers on the Performance of $CsPbI_3$-Based Perovskite Solar Cells: A Numerical Investigation in DFT, SCAPS-1D, and WxAMPS Frameworks. *ACS Omega* **2022**, *7* (47), 43210−43230.
(7) Rödel, J.; Jo, W.; Seifert, K. T. P.; Anton, E.-M.; Granzow, T.; Damjanovic, D. Perspective on the Development of Lead-Free Piezoceramics. *J. Am. Ceram. Soc.* **2009**, *92* (6), 1153−1177.
(8) Zhang, Q.; Li, Z.; Li, F.; Xu, Z.; Yao, X. Temperature Dependence of Dielectric/Piezoelectric Properties of (1-x)Bi-$(Mg_{1/2}Ti_{1/2})O_3$-$XPbTiO_3$ Ceramics with an MPB Composition. *J. Am. Ceram. Soc.* **2010**, *93* (10), 3330−3334.
(9) Hu, P.; Chen, J.; Deng, J.; Xing, X. Thermal Expansion, Ferroelectric and Magnetic Properties in (1 -x)$PbTiO_{3-x}$Bi-$(Ni_{1/2}Ti_{1/2})O_3$. *J. Am. Chem. Soc.* **2010**, *132* (6), 1925−1928.
(10) Huang, C.-C.; Cann, D. P. Phase Transitions and Dielectric Properties in $Bi(Zn_{1/2}Ti_{1/2})O_3$-$BaTiO_3$ Perovskite Solid Solutions. *J. Appl. Phys.* **2008**, *104* (2), 024117.
(11) Cooper, V. R.; Henry, A. S.; Takagi, S.; Singh, D. J. First Principles Prediction of a Morphotropic Phase Boundary in the $Bi(Zn_{1/2}Ti_{1/2})O_3$-$(Bi_{1/2}Sr_{1/2})(Zn_{1/2}Nb_{1/2})O_3$ Alloy. *Appl. Phys. Lett.* **2011**, *98* (12), 122903.
(12) Yu, R.; Matsuda, N.; Tominaga, K.; Shimizu, K.; Hojo, H.; Sakai, Y.; Yamamoto, H.; Oka, K.; Azuma, M. High-Temperature Monoclinic Cc Phase with Reduced c/a Ratio in Bi-Based Perovskite Compound $Bi_2ZnTi_{1-x}Mn_xO_6$. *Inorg. Chem.* **2016**, *55* (12), 6124−6129.
(13) Liu, X.; Hong, R.; Tian, C. Tolerance Factor and the Stability Discussion of ABO_3-Type Ilmenite. *J. Mater. Sci.: Mater. Electron.* **2009**, *20* (4), 323−327.
(14) Hur, N.; Park, S.; Sharma, P. A.; Ahn, J. S.; Guha, S.; Cheong, S.-W. Electric Polarization Reversal and Memory in a Multiferroic Material Induced by Magnetic Fields. *Nature* **2004**, *429* (6990), 392−395.
(15) Dho, J.; Leung, C.; MacManus-Driscoll, J.; Blamire, M. Epitaxial and Oriented $YMnO_3$ Film Growth by Pulsed Laser Deposition. *J. Cryst. Growth* **2004**, *267* (3−4), 548−553.
(16) Basher, M. K.; Hossain, M. K.; Uddin, M. J.; Akand, M. A. R.; Shorowordi, K. M. Effect of Pyramidal Texturization on the Optical Surface Reflectance of Monocrystalline Photovoltaic Silicon Wafers. *Optik* **2018**, *172*, 801−811.
(17) Tholkappiyan, R.; Vishista, K. Effect of Niobium on the Optical and Magnetic Properties of Bismuth Ferrite ($BiFeO_3$). *Adv. Sci. Eng. Med.* **2014**, *6* (3), 311−317.
(18) Dai, T.-G.; Tang, Y.-C.; Xie, L.-T.; Li, H.; Gao, X.-Q.; Song, A.; Pei, J.; Liu, H.; Zhang, B.-P. Enhanced High-Temperature Piezoelectric Properties of $Bi(Zn_{0.5}Ti_{0.5})O_3$-Modified $BiFeO_3$-$BaTiO_3$ Ceramics. *J. Mater. Sci.* **2023**, *58* (25), 10404−10416.
(19) Rahaman, M. M.; Imai, T.; Sakamoto, T.; Tsukada, S.; Kojima, S. Fano Resonance of Li-Doped $KTa_{1-x}Nb_xO_3$ Single Crystals Studied by Raman Scattering. *Sci. Rep.* **2016**, *6* (1), 23898.
(20) Rahaman, M. M.; Imai, T.; Miyazu, J.; Kobayashi, J.; Tsukada, S.; Helal, M. A.; Kojima, S. Relaxor-like Dynamics of Ferroelectric $K(Ta_{1-x}Nb_x)O_3$ Crystals Probed by Inelastic Light Scattering. *J. Appl. Phys.* **2014**, *116* (7), 074110.
(21) Rahaman, M. M.; Imai, T.; Kobayashi, J.; Kojima, S. Effect of Li-Doping on Polar-Nanoregions in $K(Ta_{1-x}Nb_x)O_3$ Single Crystals. *Jpn. J. Appl. Phys.* **2015**, *54* (10S), 10NB01.
(22) Rubel, M. H. K.; Takei, T.; Kumada, N.; Ali, M. M.; Miura, A.; Tadanaga, K.; Oka, K.; Azuma, M.; Yashima, M.; Fujii, K.; Magome, E.; Moriyoshi, C.; Kuroiwa, Y.; Hester, J. R.; Avdeev, M. Hydrothermal Synthesis, Crystal Structure, and Superconductivity of a Double-Perovskite Bi Oxide. *Chem. Mater.* **2016**, *28* (2), 459−465.
(23) Jiang, H.; Kumada, N.; Yonesaki, Y.; Takei, T.; Kinomura, N.; Yashima, M.; Azuma, M.; Oka, K.; Shimakawa, Y. Hydrothermal Synthesis of a New Double Perovskite-Type Bismuthate, $(Ba_{0.75}K_{0.14}H_{0.11})BiO_3{\cdot}nH_2O$. *Jpn. J. Appl. Phys.* **2009**, *48* (1R), 010216.
(24) Rubel, M. H. K.; Miura, A.; Takei, T.; Kumada, N.; Mozahar Ali, M.; Nagao, M.; Watauchi, S.; Tanaka, I.; Oka, K.; Azuma, M.; Magome, E.; Moriyoshi, C.; Kuroiwa, Y.; Azharul Islam, A. K. M. Superconducting Double Perovskite Bismuth Oxide Prepared by a Low-Temperature Hydrothermal Reaction. *Angew. Chem.* **2014**, *126* (14), 3673−3677.
(25) Rubel, M. H. K.; Mitro, S. K.; Hossain, M. K.; Hossain, K. M.; Rahaman, M. M.; Hossain, J.; Mondal, B. K.; Akter, A.; Rahman, M. F.; Ahmed, I.; Islam, A. K. M. A. First-Principles Calculations to Investigate Physical Properties of Single-Cubic $(Ba_{0.82}K_{0.18})$-$(Bi_{0.53}Pb_{0.47})O_3$ Novel Perovskite Superconductor. *Mater. Today Commun.* **2022**, *33*, 104302.
(26) Rubel, M. H. K.; Hossain, M. A.; Hossain, M. K.; Hossain, K. M.; Khatun, A. A.; Rahaman, M. M.; Ferdous Rahman, M.; Hossain, M. M.; Hossain, J. First-Principles Calculations to Investigate Structural, Elastic, Electronic, Thermodynamic, and Thermoelectric Properties of $CaPd_3B4O_{12}$ (B = Ti, V) Perovskites. *Results Phys.* **2022**, *42*, 105977.
(27) Rubel, M. H. K.; Takei, T.; Kumada, N.; Ali, M. M.; Miura, A.; Tadanaga, K.; Oka, K.; Azuma, M.; Magomae, E.; Moriyoshi, C.; Kuroiwa, Y. Hydrothermal Synthesis of a New Bi-Based $(Ba_{0.82}K_{0.18})$-$(Bi_{0.53}Pb_{0.47})O_3$ Superconductor. *J. Alloys Compd.* **2015**, *634*, 208−214.
(28) Rubel, M. H. K.; Takei, T.; Kumada, N.; Ali, M. M.; Miura, A.; Tadanaga, K.; Oka, K.; Azuma, M.; Magome, E.; Moriyoshi, C.; Kuroiwa, Y. Hydrothermal Synthesis, Structure, and Superconductivity of Simple Cubic Perovskite $(Ba_{0.62}K_{0.38})(Bi_{0.92}Mg_{0.08})O_3$ with Tc ∼ 30 K. *Inorg. Chem.* **2017**, *56* (6), 3174−3181.
(29) Sen, S. K.; Munshi, M. R.; Kumar, A.; Mortuza, A. A.; Manir, M. S.; Islam, M. A.; Hossain, M. N.; Hossain, M. K. Structural, Optical, Magnetic, and Enhanced Antibacterial Properties of Hydrothermally Synthesized Sm-Incorporating α-MoO_3 2D-Layered Nanoplates. *RSC Adv.* **2022**, *12* (53), 34584−34600.
(30) Pan, Z.; Chen, J.; Yu, R.; Yamamoto, H.; Rong, Y.; Hu, L.; Li, Q.; Lin, K.; You, L.; Zhao, K.; Fan, L.; Ren, Y.; Kato, K.; Azuma, M.; Xing, X. Giant Polarization and High Temperature Monoclinic Phase in a Lead-Free Perovskite of $Bi(Zn_{0.5}Ti_{0.5})O_3$-$BiFeO_3$. *Inorg. Chem.* **2016**, *55* (19), 9513−9516.
(31) Abrahams, S. C.; Kurtz, S. K.; Jamieson, P. B. Atomic Displacement Relationship to Curie Temperature and Spontaneous Polarization in Displacive Ferroelectrics. *Phys. Rev.* **1968**, *172* (2), 551−553.
(32) Noheda, B.; Gonzalo, J. A.; Cross, L. E.; Guo, R.; Park, S.-E.; Cox, D. E.; Shirane, G. Tetragonal-to-Monoclinic Phase Transition in a Ferroelectric Perovskite: The Structure of $PbZr_{0.52}Ti_{0.48}O_3$. *Phys. Rev. B* **2000**, *61* (13), 8687−8695.
(33) Eitel, R. E.; Randall, C. A.; Shrout, T. R.; Park, S.-E. Preparation and Characterization of High Temperature Perovskite Ferroelectrics in the Solid-Solution (1-x)$BiScO_{3-x}$$PbTiO_3$. *Jpn. J. Appl. Phys.* **2002**, *41* (Part 1, No. 4A), 2099−2104.
(34) Zhang, S.-T.; Kounga, A. B.; Aulbach, E.; Deng, Y. Temperature-Dependent Electrical Properties of $0.94_{0.5}Na_{0.5}$ TiO_3 −0.06$BaTiO_3$ Ceramics. *J. Am. Ceram. Soc.* **2008**, *91* (12), 3950−3954.
(35) Pan, Z.; Chen, J.; Fan, L.; Zhang, J.; Zhang, S.; Huang, Y.; Liu, L.; Fang, L.; Xing, X. Enhanced Piezoelectric Properties and Thermal

https://doi.org/10.1021/acsomega.3c08072
ACS Omega 2024, 9, 9147−9160

Stability in the $(K_{0.5}Na_{0.5})NbO_3$:ZnO Lead-Free Piezoelectric Composites. *J. Am. Ceram. Soc.* **2015**, *98* (12), 3935−3941.
(36) Selbach, S. M.; Tybell, T.; Einarsrud, M.; Grande, T. The Ferroic Phase Transitions of $BiFeO_3$. *Adv. Mater.* **2008**, *20* (19), 3692−3696.
(37) Abdelkader, E.; Nadjia, L.; Naceur, B.; Favier-Teodorescu, L. Thermal, Structural and Optical Properties of Magnetic $BiFeO_3$ Micron-Particles Synthesized by Coprecipitation Method: Heterogeneous Photocatalysis Study under White LED Irradiation. *Cerâmica* **2022**, *68* (385), 84−96.
(38) Salak, A. N.; Cardoso, J. P. V.; Vieira, J. M.; Shvartsman, V. V.; Khalyavin, D. D.; Fertman, E. L.; Fedorchenko, A. V.; Pushkarev, A. V.; Radyush, Y. V.; Olekhnovich, N. M.; Tarasenko, R.; Feher, A.; Čižmár, E. Magnetic Behaviour of Perovskite Compositions Derived from $BiFeO_3$. *Magnetochemistry* **2021**, *7* (11), 151.
(39) Shvartsman, V. V.; Khalyavin, D. D.; Olekhnovich, N. M.; Pushkarev, A. V.; Radyush, Y. V.; Salak, A. N. Spontaneous and Induced Ferroelectricity in the $BiFe_{1-x}Sc_xO_3$ Perovskite Ceramics. *Phys. Status Solidi* **2021**, *218* (19), 2100173.
(40) Fertman, E. L.; Fedorchenko, A. V.; Čižmár, E.; Vorobiov, S.; Feher, A.; Radyush, Y. V.; Pushkarev, A. V.; Olekhnovich, N. M.; Stanulis, A.; Barron, A. R.; Khalyavin, D. D.; Salak, A. N. Magnetic Diagram of the High-Pressure Stabilized Multiferroic Perovskites of the $BiFe_{1-Y}Sc_yO_3$ Series. *Crystals* **2020**, *10* (10), 950.
(41) Zhu, C. M.; Wang, L. G.; Tian, Z. M.; Luo, H.; Bao, D. L. G. C.; Yin, C. Y.; Huang, S.; Yuan, S. L. Effect of Annealing Temperature on the Multiferroic Properties of $0.7BiFeO_3-0.3Bi_{0.5}Na_{0.5}TiO_3$ Solid Solution Prepared by Sol-Gel Method. *Ceram. Int.* **2016**, *42* (3), 3930−3937.
(42) Zhu, L.-F.; Zhang, B.-P.; Li, S.; Zhao, L.; Wang, N.; Shi, X.-C. Enhanced Piezoelectric Properties of $Bi(Mg_{1/2}Ti_{1/2})O_3$ Modified $BiFeO_3$-$BaTiO_3$ Ceramics near the Morphotropic Phase Boundary. *J. Alloys Compd.* **2016**, *664*, 602−608.
(43) Zheng, T.; Wu, J.; Xiao, D.; Zhu, J. Recent Development in Lead-Free Perovskite Piezoelectric Bulk Materials. *Prog. Mater. Sci.* **2018**, *98*, 552−624.
(44) Tao, H.; Wu, J. Giant Piezoelectric Effect and High Strain Response in $(1-x)(K_{0.45}Na_{0.55})(Nb1Sb)O_3$ -$XBi_{0.5}Na_{0.5}Zr_1$-XHf O_3 Lead-Free Ceramics. *J. Eur. Ceram. Soc.* **2016**, *36* (7), 1605−1612.
(45) Khan, S.; Hossain, M. K. Classification and Properties of Nanoparticles. In *Nanoparticle-Based Polymer Composites*; Elsevier, 2022; pp 15−54.
(46) Salak, A. N.; Shvartsman, V. V.; Cardoso, J. P.; Pushkarev, A. V.; Radyush, Y. V.; Olekhnovich, N. M.; Khalyavin, D. D.; Vieira, J. M.; Čižmár, E.; Feher, A. The Orthorhombic-Tetragonal Morphotropic Phase Boundary in High-Pressure Synthesized $BiMg_{0.5}Ti_{0.5}O_3$-$BiZn_{0.5}Ti_{0.5}O_3$ Perovskite Solid Solutions. *J. Phys. Chem. Solids* **2022**, *161*, 110392.
(47) Lin, W.; Yang, Q.; Meng, B.; Ping, X.; Fang, C.; Zhang, H.; Chen, Y. Microstructure and Dielectric Properties of $Bi(Li_{0.5}Ta_{0.5})O_3$-Modified $Ba_{0.6}Sr_{0.4}Ti_{0.7}Zr_{0.3}O_3$-Based Ceramics. *J. Mater. Sci.: Mater. Electron.* **2023**, *34* (6), 554.
(48) Cheng, J.; Eitel, R.; Li, N.; Cross, L. E. Structural and Electrical Properties of $(1-x)Bi(Ga_{1/4}Sc_{3/4})O_3$-$XPbTiO_3$ Piezoelectric Ceramics. *J. Appl. Phys.* **2003**, *94* (1), 605−609.
(49) Jiang, Y.; Zhao, Y.; Qin, B.; Jiang, Y.; Shi, W.; Li, L.; Xiao, D.; Zhu, J. Dielectric and Piezoelectric Properties of $(1-x)(Bi_{1-y}Li_y)$-$(Sc_{1-y}Sb_y)O_3$-$XPbTiO_3$ High-Temperature Relaxor Ferroelectric Ceramics. *Appl. Phys. Lett.* **2008**, *93* (2), 022904.
(50) Momma, K.; Izumi, F. VESTA: A Three-Dimensional Visualization System for Electronic and Structural Analysis. *J. Appl. Crystallogr.* **2008**, *41* (3), 653−658.
(51) Bokuniaeva, A. O.; Vorokh, A. S. Estimation of Particle Size Using the Debye Equation and the Scherrer Formula for Polyphasic TiO_2 Powder. *J. Phys.: Conf. Ser.* **2019**, *1410* (1), 012057.
(52) Flint, L. E.; Flint, A. L. 2.3 Porosity. In *Methods of Soil Analysis: Part 4, Physical Methods*; *Soil Science Society of America Book Series*; Wiley Online Library, 2018; pp 241−254.
(53) Kumar, A.; Kumari, S.; Kumar, V.; Kumar, P.; Thakur, V. N.; Kumar, A.; Goyal, P. K.; Arya, A.; Sharma, A. L. Synthesis, Phase Confirmation and Electrical Properties of (1 - x)KNNS-xBNZSH Lead-Free Ceramics. *J. Mater. Sci.: Mater. Electron.* **2022**, *33* (9), 6240−6252.
(54) Sankur, B. Survey over Image Thresholding Techniques and Quantitative Performance Evaluation. *J. Electron. Imaging* **2004**, *13* (1), 146.
(55) Yamaguchi, O.; Narai, A.; Komatsu, T.; Shimizu, K. Crystallization and Transformation of Distorted Cubic $PbTiO_3$. *J. Am. Ceram. Soc.* **1986**, *69* (10), C-256−C-257.
(56) Kazhugasalamoorthy, S.; Jegatheesan, P.; Mohandoss, R.; Giridharan, N. V.; Karthikeyan, B.; Joseyphus, R. J.; Dhanuskodi, S. Investigations on the Properties of Pure and Rare Earth Modified Bismuth Ferrite Ceramics. *J. Alloys Compd.* **2010**, *493* (1−2), 569−572.
(57) Mallahi, M.; Shokuhfar, A.; Vaezi, M. R.; Esmaeilirad, A.; Mazinani, V. Synthesis and Characterization of Bismuth Oxide Nanoparticles via Sol-Gel Method. *Am. J. Eng. Res.* **2014**, *3* (4), 162−165.
(58) Wang, S. X.; Jin, C. C.; Qian, W. J. Bi_2O_3 with Activated Carbon Composite as a Supercapacitor Electrode. *J. Alloys Compd.* **2014**, *615*, 12−17.
(59) Zandi, S.; Kameli, P.; Salamati, H.; Ahmadvand, H.; Hakimi, M. Microstructure and Optical Properties of ZnO Nanoparticles Prepared by a Simple Method. *Phys. B: Condens. Matter* **2011**, *406* (17), 3215−3218.
(60) Galván-Ruiz, M.; Hernández, J.; Baños, L.; Noriega-Montes, J.; Rodríguez-García, M. E. Characterization of Calcium Carbonate, Calcium Oxide, and Calcium Hydroxide as Starting Point to the Improvement of Lime for Their Use in Construction. *J. Mater. Civ. Eng.* **2009**, *21* (11), 694−698.
(61) Rezaei, M.; Khajenoori, M.; Nematollahi, B. Synthesis of High Surface Area Nanocrystalline MgO by Pluronic P123 Triblock Copolymer Surfactant. *Powder Technol.* **2011**, *205* (1−3), 112−116.
(62) Song, G.; Ma, S.; Tang, G.; Wang, X. Ultrasonic-Assisted Synthesis of Hydrophobic Magnesium Hydroxide Nanoparticles. *Colloids Surf. A Physicochem.* **2010**, *364* (1−3), 99−104.
(63) Apte, S. K.; Naik, S. D.; Sonawane, R. S.; Kale, B. B.; Baeg, J. O. Synthesis of Nanosize-Necked Structure α- and γ-Fe_2O_3 and its Photocatalytic Activity. *J. Am. Ceram. Soc.* **2007**, *90* (2), 412−414.
(64) Yacob, A. R.; Mustajab, M. K. A. A.; Samadi, N. S. Calcination Temperature of Nano MgO Effect on Base Transesterification of Palm Oil. *Int. J. Chem. Mol. Eng.* **2009**, *3* (8), 408−412.
(65) Pati, D. K.; Das, P. R.; Padhee, R. Structural, Optical, Electrical and Magnetic Characteristics of Multiferroic $[Pb(Fe_{0.5}Nb_{0.5})O_3]0.3$-$[(Ca_{0.2}Sr_{0.8})TiO_3]0.7$ Perovskite Ceramic Compound. *J. Mater. Sci.: Mater. Electron.* **2023**, *34* (4), 331.
(66) Ajmal, S.; Bibi, I.; Majid, F.; Ata, S.; Kamran, K.; Jilani, K.; Nouren, S.; Kamal, S.; Ali, A.; Iqbal, M. Effect of Fe and Bi Doping on $LaCoO_3$ Structural, Magnetic, Electric and Catalytic Properties. *J. Mater. Res. Technol.* **2019**, *8* (5), 4831−4842.
(67) Srivastav, S. K.; Gajbhiye, N. S. Low Temperature Synthesis, Structural, Optical and Magnetic Properties of Bismuth Ferrite Nanoparticles. *J. Am. Ceram. Soc.* **2012**, *95* (11), 3678−3682.
(68) Jabeen Fatima, M. J.; Navaneeth, A.; Sindhu, S. Improved Carrier Mobility and Bandgap Tuning of Zinc Doped Bismuth Oxide. *RSC Adv.* **2015**, *5* (4), 2504−2510.
(69) Mohanty, H. S.; Sharma, S. K.; RaviKant, R.; Kulriya, P. K.; Kumar, A.; Thomas, R.; Pradhan, D. K. Enhanced Functional Properties of Soft Polymer-Ceramic Composites by Swift Heavy Ion Irradiation. *Phys. Chem. Chem. Phys.* **2019**, *21* (44), 24629−24642.
(70) Mohanty, B.; Parida, B. N.; Parida, R. K. Multiferroic and Optical Spectroscopic Behavior of BST in BFO Environment. *J. Mater. Sci.: Mater. Electron.* **2019**, *30* (10), 9211−9218.
(71) Rahman, M. F.; Habib, M. J. A. A.; Ali, M. H.; Rubel, M. H. K. K.; Islam, M. R.; Md. Ismail, A. B.; Hossain, M. K. Design and Numerical Investigation of Cadmium Telluride (CdTe) and Iron

https://doi.org/10.1021/acsomega.3c08072
ACS Omega 2024, 9, 9147−9160

Silicide ($FeSi_2$) Based Double Absorber Solar Cells to Enhance Power Conversion Efficiency. *AIP Adv.* **2022**, *12* (10), 105317.
(72) Hossain, M. K.; Toki, G. I.; Kuddus, A.; Mohammed, M. K. A.; Pandey, R.; Madan, J.; Bhattarai, S.; Rahman, M. F.; Dwivedi, D. K.; Amami, M.; Bencherif, H.; Samajdar, D. P. Optimization of the Architecture of Lead-Free $CsSnCl_3$-Perovskite Solar Cells for Enhancement of Efficiency: A Combination of SCAPS-1D and WxAMPS Study. *Mater. Chem. Phys.* **2023**, *308*, 128281.
(73) Wang, Y.; Miska, P.; Pilloud, D.; Horwat, D.; Mücklich, F.; Pierson, J. F. Transmittance Enhancement and Optical Band Gap Widening of Cu_2O Thin Films after Air Annealing. *J. Appl. Phys.* **2014**, *115* (7), 073505.
(74) Pervez, M. F.; Mia, M. N. H.; Hossain, S.; Saha, S. M. K.; Ali, M. H.; Sarker, P.; Hossain, M. K.; Matin, M. A.; Hoq, M.; Chowdhury, M. A. M. Influence of Total Absorbed Dose of Gamma Radiation on Optical Bandgap and Structural Properties of Mg-Doped Zinc Oxide. *Optik* **2018**, *162*, 140−150.
(75) Hossain, M. K.; Arnab, A. A.; Toki, G. F. I.; Bhattarai, S.; Tawfeek, A. M.; Bencherif, H.; Dwivedi, D. K.; Madan, J.; Pandey, R. High-Efficiency Lead-Free La_2NiMnO_6 -Based Double Perovskite Solar Cell by Incorporating Charge Transport Layers Composed of WS_2, ZnO, and Cu_2 $FeSnS_4$. *Energy Fuels* **2023**, *37* (24), 19898−19914.
(76) Rahman, M. F.; Alam Moon, M. M.; Hossain, M. K.; Ali, M. H.; Haque, M. D.; Kuddus, A.; Hossain, J.; Md. Ismail, A. B. Concurrent Investigation of Antimony Chalcogenide (Sb_2Se_3 and Sb_2S_3)-Based Solar Cells with a Potential WS_2 Electron Transport Layer. *Heliyon* **2022**, *8* (12), No. e12034.
(77) Abdullah, O. G.; Aziz, S. B.; Omer, K. M.; Salih, Y. M. Reducing the Optical Band Gap of Polyvinyl Alcohol (PVA) Based Nanocomposite. *J. Mater. Sci.: Mater. Electron.* **2015**, *26* (7), 5303−5309.
(78) Mostafa, N. Y.; Badawi, A.; Ahmed, S. I. Influence of Cu and Ag Doping on Structure and Optical Properties of In_2O_3 Thin Film Prepared by Spray Pyrolysis. *Results Phys.* **2018**, *10* (April), 126−131.
(79) Hareesh, K.; Sanjeev, G.; Pandey, A. K.; Rao, V. Characterization of UV-Irradiated Lexan Polycarbonate Films. *Iran. Polym. J.* **2013**, *22* (5), 341−349.
(80) Ahad, A.; Taher, M. A.; Das, M. K.; Rahaman, M. Z.; Khan, M. N. I. Effect of Y Substitution on Magnetic and Transport Properties of $Ba_{0.95}La_{0.05}Ti_{1-x}Y_xO_3$ Ceramics. *Results Phys.* **2019**, *12* (February), 1925−1932.
(81) Tahalyani, J.; Rahangdale, K. K.; K, B. The Dielectric Properties and Charge Transport Mechanism of π-Conjugated Segments Decorated with Intrinsic Conducting Polymer. *RSC Adv.* **2016**, *6* (74), 69733−69742.
(82) Nadeem, M.; Khan, W.; Khan, S.; Husain, S.; Ansari, A. Tailoring Dielectric Properties and Multiferroic Behavior of Nanocrystalline $BiFeO_3$ via Ni Doping. *J. Appl. Phys.* **2018**, *124* (16), 164105.
(83) Kaur, M.; Uniyal, P. Study on Structural, Multiferroic, Optical and Photocatalytic Properties of Ferroelectromagnetic Nanoparticles: $Bi_{0.9}Ba_{0.1}Fe_{0.8}Ti_{0.2}O_3$. *J. Supercond. Nov. Magn.* **2017**, *30* (2), 431−439.
(84) Peelamedu, R.; Grimes, C.; Agrawal, D.; Roy, R.; Yadoji, P. Ultralow Dielectric Constant Nickel-Zinc Ferrites Using Microwave Sintering. *J. Mater. Res.* **2003**, *18* (10), 2292−2295.
(85) Devan, R. S.; Chougule, B. K. Effect of Composition on Coupled Electric, Magnetic, and Dielectric Properties of Two Phase Particulate Magnetoelectric Composite. *J. Appl. Phys.* **2007**, *101* (1), 014109.
(86) Topal, U. Coexistence of Ferromagnetism and Diamagnetism in Y-Ba-Zn-O Compound. *J. Supercond. Nov. Magn.* **2011**, *24* (1−2), 957−959.
(87) Wang, W.; Xu, L.; Zhang, R.; Xu, J.; Xian, F.; Su, J.; Yang, F. Coexistence of Ferromagnetism and Paramagnetism in ZnO/CuO Nanocomposites. *Chem. Phys. Lett.* **2019**, *721*, 57−61.
(88) Thakur, G. S.; Fuchs, G.; Nenkov, K.; Haque, Z.; Gupta, L. C.; Ganguli, A. K. Coexistence of Superconductivity and Ferromagnetism in $Sr_{0.5}Ce_{0.5}FBiS_{2-X}Se_x$ (x = 0.5 and 1.0), a Non-U Material with Tc < TFM. *Sci. Rep.* **2016**, *6* (1), 37527.

https://doi.org/10.1021/acsomega.3c08072
ACS Omega 2024, 9, 9147−9160